Experimental closed-loop flow separation control: Data- and phenomenological-driven approaches

T. Arnoult, G. Acher, V. Nowinski, P. Vuillemin, C. Briat, P. Pernod, C. Ghouila-Houri, A. Talbi, E. Garnier, C. Poussot-Vassal

European Journal of Control 79 (2024) 101082

Contents lists available at ScienceDirect

European Journal of Control

journal homepage: www.sciencedirect.com/journal/european-journal-of-control

Experimental closed-loop flow separation control: Data- and phenomenological-driven approaches

T. Arnoult [a], G. Acher [b], V. Nowinski [b], P. Vuillemin [c], C. Briat [d], P. Pernod [a], C. Ghouila-Houri [a], A. Talbi [a], E. Garnier [b], C. Poussot-Vassal [c,*]

[a] Univ. Lille, CNRS, Centrale Lille, Univ. Polytechnique Hauts-de-France, UMR 8520 - IEMN - Institut d'Electronique de Microélectronique et de Nanotechnologie, F-59000 Lille, France

[b] Univ. Lille, CNRS, ONERA, Arts et Metiers Institute of Technology, Centrale Lille, UMR 9014, Laboratoire de Mécanique des fluides de Lille-Kampé de Fériet, F-59000 Lille, France

[c] DTIS, ONERA, Université de Toulouse, 31000, Toulouse, France

[d] D-BSSE, ETH Zürich, Switzerland

ARTICLE INFO

Recommended by T. Parisini

Keywords:
Flow control
Data-driven control
Positive control
Wind tunnel test

ABSTRACT

Flow control aims at modifying a natural flow state to reach an other flow state considered as advantageous. In this paper, active feedback flow separation control is investigated with two different closed-loop control strategies, involving a reference signal tracking architecture. Firstly, a data-driven control law, leading to a linear (integral) controller is employed. Secondly, a phenomenological/model-driven approach, leading to a non-linear positive (integral) control strategy is investigated. While the former benefits of a tuning simplicity, the latter prevents undesirable effects and formally guarantees closed-loop stability. Both control approaches were validated through wind tunnel experiments of flow separation control over a movable NACA 4412 plain flap. These control laws were designed with respect to hot-film measurements, performed over the flap for different deflection angles. Both control approaches proved efficient in avoiding flow separation. The main contribution of this work stands in providing practitioners, simple but yet efficient control design methods for the flow separation phenomena. Equivalently important, a complete validation campaign data-set is also provided.

1. Introduction

1.1. Forewords on flow separation objective

Flow separation over an aircraft flap is characterized by a decrease in the lift coefficient, an increase in the drag coefficient and can occur during the critical take-off and landing phases. Most aircraft circumvent this issue using slotted flaps, which however add structural weight and complicate the maintenance. Therefore, one solution would be to simplify these structures into plain flaps with integrated flow control devices to avoid flow separation.

Flow control consists in modifying a flow general behavior with a space localized perturbation, in order to reach a flow configuration considered as favorable. In that sense, flow control can help reducing noise radiation, delaying the laminar-turbulent boundary layer transition or can help avoiding flow separation (Gad-el Hak, 2000). Flow control methods can be categorized as passive or active methods. Passive methods do not require any external source of energy to act on the flow. One may mention passive vortex generators, which have been widely used to prevent flow separation on aircraft wings. Vortices generated by these devices help re-energizing the boundary layer and therefore prevent its separation. However, they act permanently on the flow, even at off-points design. In that sense, an active flow control method can be employed in a closed-loop strategy as considered in this study. The actuators command can therefore be adapted depending on the needs. The closed-loop control of flow separation can ensure the optimization of aerodynamic performances of an airplane. For such a flow control objective, as the base flow to reach does not exist without external forcing, the closed-loop control strategy helps maintaining the attached flow state. Closed-loop can also guarantee the system robustness towards external disturbances such as variations of the flow properties due to its turbulent nature or towards gusts and wind shears that airplanes can undergo during take-off and landing phases.

As discussed by Pastoor, Henning, Noack, King, and Tadmor (2008), closed-loop approaches can be classified depending on their complexity. These different strategies have been used regarding the closed-loop

* Corresponding author.
E-mail address: charles.poussot-vassal@onera.fr (C. Poussot-Vassal).

https://doi.org/10.1016/j.ejcon.2024.101082
Received 20 December 2023; Received in revised form 24 May 2024; Accepted 29 June 2024
Available online 9 July 2024

control of flow separation and separated flow. They can rely on triggering, which consists in turning on the actuators when a threshold value, related to a predefined criterion of the flow state is exceeded, e.g. onset of flow separation, minimum amount of lift acceptable (Benard, Cattafesta, Moreau, Griffin, & Bonnet, 2011; Lombardi, Bowles, & Corke, 2013; Packard & Bons, 2012; Poggie et al., 2010; Rethmel et al., 2011; Tewes, Wygnanski, & Washburn, 2011) or on the use of PID controllers (Allan et al., 2000; Lee et al., 2013; Pinier, Ausseur, Glauser, & Higuchi, 2007; Shaqarin, Braud, Coudert, & Stanislas, 2013; Troshin & Seifert, 2013), slope and extremum seeking algorithms (Becker, King, Petz, & Nitsche, 2007; Benard, Moreau, Griffin, & Cattafesta III, 2010; Chabert, Dandois, & Garnier, 2014; Feingesicht, Polyakov, Kerhervé, & Richard, 2017; Garwon, Darmadi, Urzynicok, Barwolff, & King, 2003; Tian, Cattafesta, & Mittal, 2006) or model-based controller design techniques (Henning & King, 2007; King, Heinz, Bauer, Grund, & Nitsche, 2013) and machine learning approaches (Debien et al., 2016; Gautier et al., 2015; Shimomura, Sekimoto, Oyama, Fujii, & Nishida, 2020). A first simple closed-loop approach is the triggering strategy. Poggie et al. (2010) employed the triggering method based on hot-films sensors RMS (root mean square) value for the control of a separated flow. The control is implemented with a plasma actuator in the form of a single DBD (Dielectric Barrier Discharge). This type of actuator consists in two electrodes separated by a dielectric layer. The bottom electrode is connected to the ground, while the exposed one is supplied with an AC high voltage in the range of kV with a frequency in the range of kHz. The ambient air is ionized by the electrodes and an electrohydrodynamic force is induced. Using this actuator, the model sectional lift coefficient was increased of 10% for a freestream Mach number M_∞ of 0.05, when the separation point reached a position defined as the limit. In a similar approach, Benard et al. (2011) also highlight the benefits of hysteresis regarded the flow separation control over a NACA 0015 airfoil. The triggering of a single DBD actuator is based on the pressure coefficient rms, used as the flow separation predictor. On their side, Rethmel et al. (2011) used nanosecond-pulse driven DBD actuators placed on a NACA 0015 airfoil to control flow separation for Mach numbers up to 0.26. Control is triggered when a threshold power dissipated by the hot-film is overcome. The DBD actuators, in this case, do not induce a ionic wind as a forcing but rather set off a thermal exchange with the boundary layer exciting its instabilities. Despite the interest of the triggering method lies in its simple implementation, definitions of the threshold value is highly dependent on the experimental conditions and the closed-loop control implementation does not guarantee the control robustness towards external disturbances.

PID controllers have also been used for such applications of flow control. Shaqarin et al. (2013) and Allan et al. (2000) respectively implemented a proportional and a PID controller on a descendant ramp and a hump, both obstacles provoking the flow separation. Allan et al. (2000), using a siren type valve generating pressure oscillations, demonstrated that considering a PID controller, the integral action was the most effective to track the reference value of pressure coefficient, while the proportional or derivative parts amplified the oscillations induced by the flow fluctuations. Troshin and Seifert (2013), Lee et al. (2013) and Pinier et al. (2007) implemented PID controllers on airfoil with synthetic jets and respectively targeting either to control lift, the pressure coefficient or delay the onset of separation using pressure measurements. Synthetic jets alternate blowing and air sucking phases to induce flow velocity fluctuations. These type of actuators have a limited bandwidth as their actuation frequency must be close to the actuator resonant frequency. Indeed, the induced velocity by synthetic jets is maximum near their resonance and rapidly decays for actuation frequencies away from the resonance. Regarding the study of Garwon et al. (2003), an adaptive integral controller is implemented on a backward facing step for a freestream velocity of 3 m/s. Control is performed using a loudspeaker placed at the step leading edge and pressure measurements are realized to determine the length of the re-circulation area. Although PID controllers have been widely used for the closed-loop control of several flow problems, the PID parameters optimization might be time-consuming. One way to circumvent this issue is proposed by Killingsworth and Krstic (2006), who propose the optimization of PID controllers based on an internal closed-loop method exploiting extremum seeking.

Extremum and slope seeking algorithms have been widely used for the control of flow separation. Benard et al. (2010) and Chabert, Dandois, and Garnier (2014) both used a slope seeking algorithm respectively on a NACA 0015 airfoil for Reynolds numbers between $1.3{\cdot}10^5$ and $4{\cdot}10^5$ and on a NACA 4412 plain flap for $Re_c = 2{\cdot}10^6$. Benard et al. (2010) aim at maximizing the airfoil lift based on the use of a single DBD actuator and a balance for the measurements. The controller robustness is also shown through dynamics closed-loop experiments, despite a long loop time due to the balance. Slope seeking is based on the presence of a gradient of the static map in the controlled value. An improved version of slope seeking is proposed by Dandois and Pamart (2013), who integrated an adaptive gain to the algorithm ensuring an optimal performance of the gradient estimation. This numerical study, implements the method on a rounded ramp with synthetic jet for a freestream Mach number $M_\infty = 0.31$. This improved methodology was used by Chabert, Dandois, and Garnier (2014), with the loop gain adapted by a fuzzy-logic regulator. This technique enables a faster convergence of the control resulting in less power consumption by the actuators. Using extremum seeking on a high lift configuration, Becker et al. (2007) implemented a MIMO approach. Compared to the SISO method also employed in that study, the MIMO scheme achieved the best lift gains. The control is implemented using pulsed jets induced by solenoid valves, while the lift is derived from pressure measurements. Another adaptive control method of separated flow is proposed by Tian et al. (2006), who considered a NACA 0025 airfoil for $Re_c = 10^5$ equipped with synthetic jets. The control is performed using a quasi-static adaptive nonlinear control scheme based on the downhill simplex algorithm. In this study, despite the non linear of the actuators driven with modulated signals, it is shown that the maximization of the lift to drag ratio depends on the forcing of the non linear interactions between the shear layer and the wake instabilities. As discussed by Brunton and Noack (2015), extremum seeking algorithm is attractive for the closed-loop control of complex systems, as such a methodology does not rely on an underlying system. Nevertheless, extremum seeking algorithms are characterized by slower converging time compared to model-based approaches (Chabert, 2014).

Model-based controller design techniques have also been used for the control of separated flow. Henning and King (2007) used the robust $\mathcal{H}_\infty$ design technique to control the re-circulation flow length behind a backward facing step characterized by $Re_H = 25000$ (H being the step height). An array of pressure sensors is used in combination with slot hose loudspeakers for the MIMO closed-loop implementation. The black box model is identified during step experiments, yielding linear time-continuous multi-variable models. The designed controller is then employed to impose the re-circulation flow length and for disturbance rejection. Using the similar controller design technique, King et al. (2013) on an airbus half-size model and on a Stemme S10 glider. Both the model and the glider were equipped with pulsed jets driven by solenoid valves and pressure measurements for the monitoring of lift. Both SISO and MIMO controls are implemented. For both the wind tunnel and in-flight experiments, models of the flow dynamics are derived using PRBS as input for the actuators. The controllers then designed were used to both reject disturbances and control lift.

More recently, further model-free approaches have been considered based on machine learning. Gautier et al. (2015) and Debien et al. (2016) both used genetic programming for the control of separated flows, respectively considering a backward facing step with $Re_H = 1350$ and a sharp edge ramp for $Re_\theta = 3500$. Both studies aimed at the minimization of the re-circulation flow area. Gautier et al. (2015) controlled the flow using slotted jets based on on-line PIV measurements, determining the re-circulation bubble size, while Debien et al. (2016)

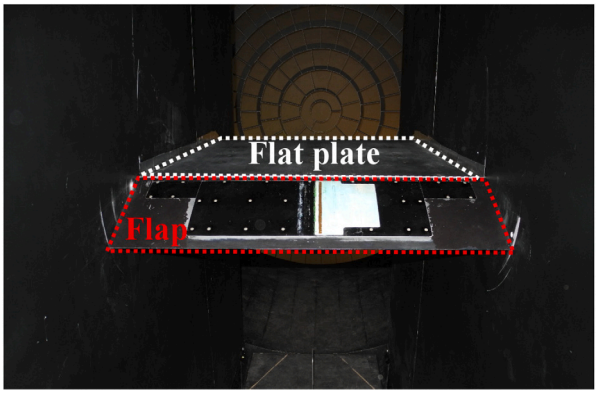

Fig. 1. Wind tunnel facility view (Onera, Lille, France). The commanded horizontal wing is in between the two vertical structures. The flow is longitudinally traveling from the back of the photo.

used vortex generators supplied by solenoid valves coupled with wall shear stress measurements. Use of deep reinforcement learning was achieved by Shimomura et al. (2020) on a NACA 0015 airfoil with $Re_c = 63000$. The control is based on the use of a single DBD actuator and on pressure measurements with the aim of reattaching the separated flow. As discussed by Gautier et al. (2015), deep reinforcement machine learning and genetic programming require a large number of experiments to complete criteria of statistical convergence, therefore limiting their application to experimental flow control.

1.2. Contribution statement

The contribution of the paper is to deploy and evaluate in an experimental wind tunnel facility, involving a NACA 4412 plain flap airfoil, two active closed-loop control design strategies to drive the flow separation phenomena. The first one is a (model-free) *linear data-driven* approach, while the second one is a *positive nonlinear phenomenological/model-driven* strategy. The data-driven rationale is extensively detailed in Kergus (2019), while the positive strategy is discussed in Briat (2020), initially considered for the control of biological systems in Briat, Gupta, and Khammash (2016). Both control methods are based on the use of on/off solenoid valves as actuators and on hot-film sensors. Both control structure involve the same reference signal to track, which value is also discussed. Each strategy is validated in a wind tunnel facility (see Fig. 1) and leads to a lift increase, and cancelled/reduced flow separation.

As a glimpse of this paper result, Fig. 2 illustrates the lift performances with and without flow separation control. In addition, Fig. 3 illustrates the closed-loop frequency response (obtained with a frequency sweeping reference signal) for varying flap angles, with respect to the reference objective transfer. The rest of this note details the process for reaching such performances and derives a generic but yet simple approach to design and validate two flow separation feedback control laws. We believe that the proposed rationales are sufficiently simple to be applied on a variety of similar setups.

1.3. Notations and paper organization

After recalling the flow separation problem in Sections 1, 2 presents the considered experimental setup. Both linear data-driven and nonlinear positive model-driven flow control designs are recalled and validated in Section 3. Conclusions and outlooks are gathered in Section 4.

By $\mathbb{R}$, $\mathbb{Z}$ and $\mathbb{N}$ we indicate the sets of real, integer and natural (positive integer) numbers, respectively. The LTI dynamical system $\mathbf{K}$ pencil is denoted $\Lambda_{\mathbf{K}}$. We denote with $h \in \mathbb{R}_+$, the sampling-time, with

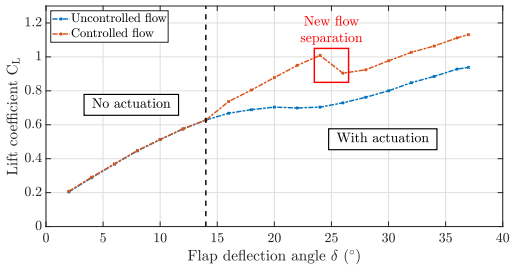

Fig. 2. Evolution of the lift coefficient C_L without (blue curve) and with (red curve) control against the flap deflection angle δ for $U_\infty = 34.5$ m/s.

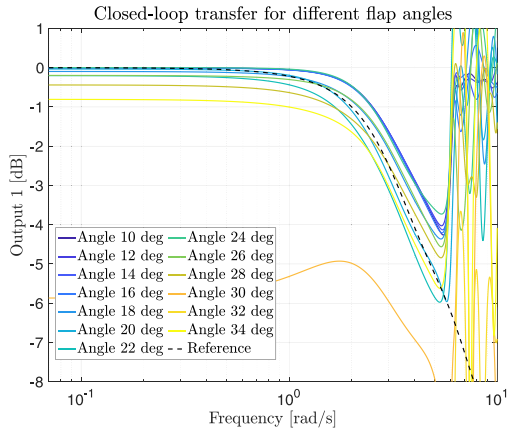

Fig. 3. Frequency-domain responses of the controlled system for $U_\infty = 34.5$ m/s. Colored solid lines (response for different flap deflection angle δ) and reference (dashed black).

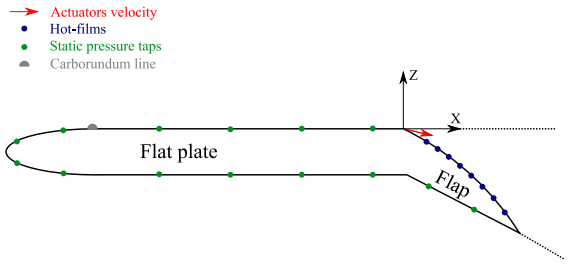

Fig. 4. Sketch of the plain flap configuration (only few pressure taps are sketched).

I the identity matrix and $\imath$ ($\sqrt{\imath} = -1$) the complex variable. The time average of a quantity is denoted $\langle\rangle$. Regarding the model, c_{flap} and c_{tot} respectively stand for the flap chord length and the model total length. The flap deflection angle is denoted δ. The freestream velocity is noted U_∞ and the Reynolds number based on the model total length is computed as $Re = U_\infty c_{\text{tot}}/\nu$, with ν the air kinematic viscosity. Considering the actuators, f, f^+ and α refer to the actuation frequency, its reduced form and to the duty cycle. The momentum coefficient C_μ is derived from q_{jet}, U_{jet}, ρ_∞ and A_{ref} respectively the actuators mass flow rate, actuators outlet velocity, freestream density and reference area chosen as the flap area. Concerning the sensors setup, the pressure coefficient C_p calculation is based on the static pressure p and the freestream pressure p_∞. The flap lower and upper surfaces pressure coefficients are denoted $C_{p_{\text{lower}}}$ and $C_{p_{\text{upper}}}$. These coefficients help computing the lift coefficient C_L as detailed in the following. In some of the following figures considering the controlled case, zones without and with actuation are distinguished. They respectively denote cases in which the control is applied but valves are not actuated or actuated with a duty cycle fixed by the controller.

2. Experimental control setup description

2.1. Setup overview and wing surface properties

Flow control experiments were carried out in the L1 wind tunnel facility at ONERA, Lille. It is characterized by a test section diameter of 2.40 m. The model is composed of a 867 mm long flat plate, stabilizing the boundary layer, followed by a plain flap of chord length $c_{\text{flap}} = 220$ mm, yielding a model total length $c_{\text{tot}} = 1087$ mm. The plain flap design is based on a NACA 4412 airfoil. As depicted in Fig. 1, two lateral panels separated by 800 mm are placed inside the wind tunnel test section, next to the model borders to avoid side effects and ensure that the flow developing over the model is bi-dimensional. The flow separation control over this model has already been studied by Chabert, Dandois, and Garnier (2014), Chabert, Dandois, Garnier, and Jacquin (2014), who implemented a slope seeking control algorithm. A carborundum line is placed at the flat plate leading edge to help triggering the boundary layer transition from laminar to turbulent. The freestream velocity measurements inside the wind tunnel test section are performed with Pitot tubes. During the experiments, U_∞ is fixed to 34.5 m/s, yielding a Reynolds number based on the model total chord length c_{tot} of $Re_{c_{\text{tot}}} = 2.39 \times 10^6$. The turbulence level inside the wind tunnel is about 1.3%. The model is placed inside the test section with a 0° angle of attack. The motorized flap can be deflected downward at an angle δ varying between 2° and 37°. Note that the flap is not an actuator used in the control loop but a way to modify the configuration accounting for uncertainties and allowing exhibiting the separation phenomena (Fig. 2).

2.2. Actuators and sensors description

2.2.1. Actuation system

The actuation setup is composed of 7 slots spanning along the flap leading edge at a location of $x/c_{\text{flap}} = 0.08$. Separated by 7 mm from each other, the actuators slots are 90 mm long and 0.25 mm thick each. They cover 80% of the flap span and are supplied by on/off Festo MHE2 fast response solenoid valves, driven by square command signals and fed with pressurized air up to 7 bar. The opening and closing valves delays are respectively 1.7 ms and 2 ms, yielding actuators response 3 orders of magnitude faster than the derived system dynamics, as detailed in the following. The slot outlet velocity is inclined by 30° relatively to the flap local tangent. For a matter of actuators integration inside the model, no other orientation was tested. The valves mass flow rate and the actuation frequency are fixed respectively to $q_{jet} = 21$ g/s and to $f = 100$ Hz. Based on characterization of the actuators with hot-wire measurements, choosing an actuation frequency of 100 Hz guarantees the valves outlet velocity to evolve linearly with the duty cycle, for α ranging from 6 % to 92 %. The reduced actuation frequency referred as f^+ is therefore:

$$f^+ = \frac{f\ c_{\text{flap}}}{U_\infty} \cong 0.64. \tag{1}$$

The added momentum to the flow can be characterized by C_μ defined as:

$$C_\mu = \frac{q_{\text{jet}} U_{\text{jet}}}{\frac{1}{2}\rho_\infty U_\infty^2 A_{\text{ref}}} = \frac{\rho_{jet} U_{jet}^2 A_{jet}}{\frac{1}{2}\rho_\infty U_\infty^2 A_{ref}}. \tag{2}$$

where ρ_{act}, U_{act} and A_{jet} respectively denote the actuators air density, outlet velocity and the 7 actuators outlet total surface. The other terms ρ_∞, U_∞ and A_{ref} stand for the freestream density, velocity and for the reference area chosen as the flap area in the present case. Considering the conditions detailed above, the constant blowing momentum coefficient has a value of 1.6%.

Table 1
Positions of the hot-films with respect to the flap leading edge.

Hot-film number	Distance to the flap leading edge (mm)	Dimensionless abscissa x/c_{flap}
HF1	32.6	0.148
HF2	52.6	0.239
HF3	72.6	0.330
HF4	92.4	0.420
HF5	112.4	0.511
HF6	132.4	0.602
HF7	152.5	0.693
HF8	172.5	0.784

In the case of pulsed blowing, as in this study, the periodic momentum coefficient is defined by Greenblatt and Wygnanski (2000) as:

$$\langle C_\mu \rangle = \frac{\rho_{jet} \langle U_{jet}^2 \rangle A_{jet}}{\frac{1}{2}\rho_\infty U_\infty^2 A_{ref}}. \tag{3}$$

Similarly to Chabert (2014), given the valves square command signals it is deduced that $\langle U_{jet}^2 \rangle = \alpha U_{max}^2$, with U_{max} the valves maximal outlet velocity for the supply conditions considered. Therefore :

$$\langle C_\mu \rangle = \alpha \frac{\rho_{jet} U_{max}^2 A_{jet}}{\frac{1}{2}\rho_\infty U_\infty^2 A_{ref}} = \frac{1}{\alpha} \frac{q_{jet} \langle U_{jet} \rangle}{\frac{1}{2}\rho_\infty U_\infty^2 A_{ref}}. \tag{4}$$

The on/off valves duty cycle α denotes the control input varied with time and used to control the system during the closed-loop control implementation. During the flow control experiments $\langle C_\mu \rangle$ used reached a maximum value of 4.6%.

2.2.2. Sensing system

Regarding the sensors setup, 51 pressure taps are dispatched on both the flat plate and flap upper and lower surfaces. Two types of pressure sensors are used on the model, both characterized by a full-scale uncertainty of 0.06%. Pressure sensors placed on the model flat plate have a pressure range of 0-6895 Pa (0–1 psi) yielding an uncertainty of 4.14 Pa, while the one on the flap have a pressure range of 0-34 474 Pa (0–5 psi) yielding an uncertainty of 20.68 Pa. From these pressure measurements both the pressure coefficient at each tap location and the global lift coefficient can be computed. The pressure coefficient is defined according to the following equation:

$$C_p = \frac{p - p_\infty}{\frac{1}{2}\rho_\infty U_\infty^2}. \tag{5}$$

The lift coefficient is derived from the pressure coefficient computations according to the following formula:

$$C_L = \int_0^1 (C_{p_{\text{lower}}} - C_{p_{\text{upper}}})\, d\frac{x}{c_{\text{tot}}}. \tag{6}$$

Both quantities C_p and C_L are used to assess the control effects, comparing cases of uncontrolled and controlled flows.

2.2.3. Experimental strategy

To monitor the flow separation over the flap and implement the control part, eight Senflex® hot-films are placed along the flap chordwise direction. Positions of the hot-films with respect to the flap leading edge are presented in Table 1 and sketched in Fig. 4. Connected to two Dantec® Streamlines units, hot-films signals are recorded at a sampling frequency of 1.25 kHz over 3 min for each measurement points. The control tracking value is defined with respect to the fifth hot-film measurements, located at the dimensionless abscissa $x/c_{\text{flap}} = 0.511$, taking the coordinate origin at the flap leading edge. As described in the following section, the flow separation point reaches this sensor position for a flap deflection angle of 20°, in the middle of the flap deflection

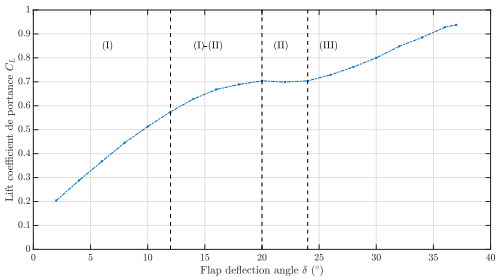

Fig. 5. Evolution of the unforced flow lift coefficient C_L against the flap deflection angle δ ($U_\infty = 34.5$ m/s).

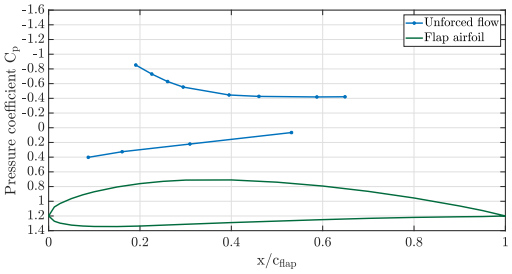

Fig. 6. Evolution of the unforced flow pressure coefficient C_p against the dimensionless abscissa x/c_{flap}. ($\delta = 18°$ and $U_\infty = 34.5$ m/s). The two curves represent the profile upper and lower coefficients.

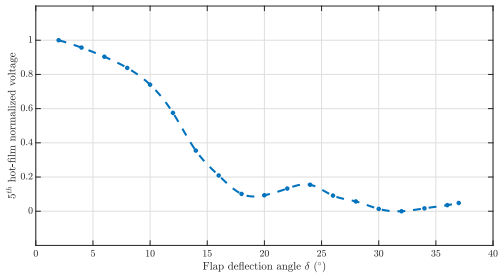

Fig. 7. Evolution of the normalized voltage of the $5th$ hot-film against the deflection angle δ ($U_\infty = 34.5$ m/s).

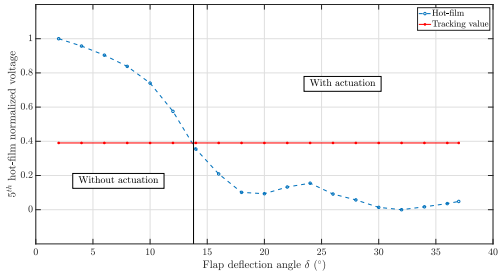

Fig. 8. Evolution of the normalized voltage of the $5th$ hot-film (blue curve) and the reference value (red curve) against the deflection angle δ ($U_\infty = 34.5$ m/s). The black curve separates areas without and with actuation.

angle range. This sensor is therefore considered ideal for the closed-loop control implementation and tests of robustness. Control scripts, written in LabVIEW Real-Time 2011 via a PXIe-8102 controller, are embedded in a PXI chassis.

2.3. Performance characterization towards specifications

First measurements focused on the unforced flow characterization. The freestream velocity was fixed to $U_\infty = 34.5$ m/s and the flap was deflected from 2° down to 37°. The evolution of the lift coefficient is presented in Fig. 5 and similar results to the one presented in Chabert, Dandois, Garnier, and Jacquin (2014) are obtained.

Following Fig. 5 and as described by Hoerner (1985), four zones can be distinguished. The first zone (I), for δ between 2° and 12°, describes a linear evolution of C_L against δ. The second zone (I)-(II) corresponds to a slower increase in the lift coefficient and spreads between 12° and 20°, indicating the development of the flow separation over the flap. The zone denoted (II) corresponds to a plateau of C_L due to the recirculation bubble entirely developed over the flap. Finally, the zone (III) denotes a zone of nonlinear increase in the lift coefficient. The nonlinear evolution of C_L in (III) would be better observed with higher deflection angles, as pointed out by Hoerner (1985).

The development of the recirculation area over the flap can also be observed in the pressure coefficient. Fig. 6 highlights the evolution of C_p against the dimensionless abscissa x/c_{flap} for a deflection angle of 18°. The pressure gradient between 0.19 and 0.46 is followed by a plateau of C_p between 0.46 and 0.65, indicating the flow separation. The longer the plateau is, the longer the flow recirculation area is. Therefore, as the flap deflection angle is increased, the C_p plateau spreads over a larger area.

Signals of the 8 hot-film sensors were also recorded during these tests. For each deflection angle, hot-films time series have been averaged and normalized according to $U^* = (\langle U \rangle - U_{min})/(U_{max} - U_{min})$, where U^* is the dimensionless hot-film voltage, $\langle U \rangle$ the hot-film mean voltage, U_{min} and U_{max} respectively are the hot-film minimum and maximum voltages. Fig. 7 depicts the evolution of U^* for the fifth hot-film on the flap, which is located at $x/c_{\text{flap}} = 0.511$. As the flap angle is increased the hot-film normalized voltage decreases. This trend indicates a decreasing wall shear stress, which reaches a local minimum for $\delta = 20°$. The first minimum at this flap angle, points out the flow separation at this location. When the flap is further deflected, the hot-film voltage increases as the flow recirculation bubble intensifies and reaches a local maximum. The voltage reaches a global minimum for an angle of $\delta = 32°$. This second minimum may be due to the apparition of a second recirculation zone occurring for high deflection angles, as observed in Chabert (2014).

2.4. Reference signal and control architecture

Following these observations, a reference value for the fifth hot-film sensor is defined, such that the flow separation over the flap is avoided. The normalized objective value U^*_{obj} is fixed to 0.3903. In Fig. 8, this reference value is superimposed with the evolution of the fifth hot-film normalized voltage. Although statistical moments derived from the hot-film measurements could be used for flow separation detection, such as in Chabert, Dandois, Garnier, and Jacquin (2014), in the present study, the aim is to present two novel closed-loop control strategies for flow separation problems. Therefore, the use of a mean value derived from the 5th hot-film is deemed sufficient for the control implementation. The controller aim is therefore to maintain the hot-film normalized voltage to the reference value. Therefore, two different zones are defined in this chart. One for deflection angles $\delta < 13.8°$ and the second one for $\delta > 13.8°$. The first one corresponds to deflection angles for which actuators do not add momentum to the flow, as the hot-film voltage is above the reference value. The second one defines angles δ for which the Festo valves are cyclically actuated and aim at maintaining the hot-film voltage to the reference value. Based on this reference value, from now on denoted $\mathbf{r}$, ability of both control strategies (either linear data-driven or positive model-driven) to maintain this value is investigated.

Based on the above considerations, a *reference signal tracking feedback control architecture* can be set up. With reference to Fig. 9, one aims at designing a h-sampled control law aiming at ensuring that the output signal $\mathbf{y}(t_k)$, measured by the fifth hot-film, tracks $\mathbf{r}(t_k)$, the

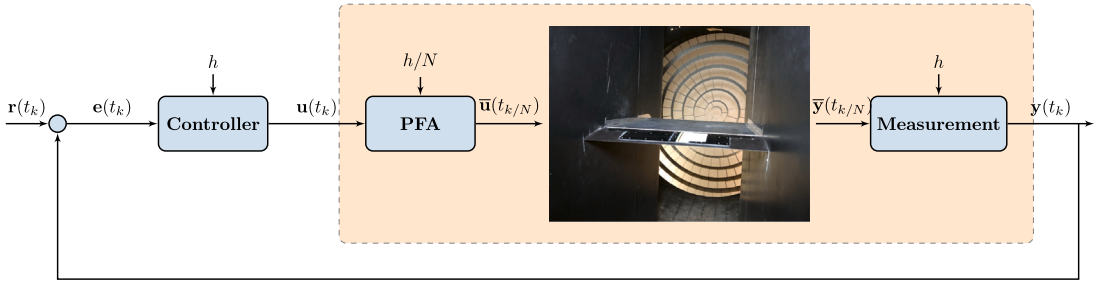

Fig. 9. Overview of the considered closed-loop architecture. The **controller**, sampled at frequency h, feeds a series of PFA acting along the wing span. The system is illustrated by the setup photo, and the measurement is achieved by the hot-films located along the wing flap. The orange block is the overall system.

reference level previously defined. The controller provides a sampled-time continuous order $\mathbf{u}(t_k)$, transformed in an on-off one $\overline{\mathbf{u}}(t_{k/N})$, leading to the controlled duty cycle α applied by the PFA (Pulsed Fluidic Actuator), sampled N times faster (see also Poussot-Vassal, Kergus, Kerhervé, Sipp, and Cordier (2022) for details on the PFA). The control problem boils down to a *reference tracking one*.

Remark 1 (*Sensor Location*)**.** In the considered experimental case, the fifth sensor is selected. However, other locations or even multiple sensors may be considered. The impact of this placement/selection may be considered in future works. The choice for this sensor was dictated by the following considerations: first, the quality of the signal was good, second, it was located far enough to actually see the separation phenomenon.

Remark 2 (*Control Architecture Extensions*)**.** Similarly, in the considered experimental context, a single input, single output controller is sought. The rest of the section sticks to this configuration. However, extensions to multi-input and single-output are possible. Extensions to multiple actuators are also possible but would lead to considerably more complex analysis.

3. Flow separation control tuning

Considering the control architecture in Fig. 9, this section details the design and tuning of the controller. Two different strategies are implemented and evaluated. First, the linear Loewner Data-Driven Control (L-DDC) (Kergus, 2019) (Section 3.1) and second, a phenomenological-driven nonlinear positive control (Briat, 2020) (Section 3.2). Both configurations performances are commented and illustrated in Section 3.3.

3.1. L-DDC design

3.1.1. Idea and principle

The L-DDC belongs to the so-called data-driven reference model approaches.[1] The L-DDC procedure boils down to two steps: first deriving the *ideal controller* denoted $\mathbf{K}^\star$, and second, the *controller identification* via interpolation in the Loewner framework (Gosea, Poussot-Vassal, & Antoulas, 2022; Mayo & Antoulas, 2007).

We recall the main steps in the SISO case and with the considered reference tracking architecture. Following Fig. 10, the objective is to find an LTI controller with transfer function $\mathbf{K} : \mathbb{C}\backslash\Lambda_{\mathbf{K}} \to \mathbb{C}$ that minimizes the transfer difference between $\mathbf{r}$ and $\boldsymbol{\varepsilon}$, *i.e.* between the resulting closed-loop and a user-defined reference model $\mathbf{M} : \mathbb{C}\backslash\Lambda_{\mathbf{M}} \to \mathbb{C}$.

[1] DDC methods have a long history dating to the proportional, integral, derivative (PID) tuning method by Ziegler–Nichols in early 40's or the self tuning regulator by Åström in the 90's (see *e.g.* Ziegler and Nichols (1942) for more details and references). This field remains still very active (see *e.g.* Formentin, van Heusden, and Karimi (2014)).

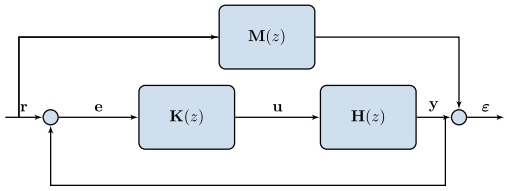

Fig. 10. Data-driven control problem formulation. z denotes the complex variable either in the continuous or sampled-time.

This is made possible through the definition of the ideal controller $\mathbf{K}^\star$, being the LTI controller that would have given the desired reference model behavior if inserted in the closed-loop. The latter is defined as $\mathbf{K}^\star = \mathbf{H}^{-1}\mathbf{M}(I-\mathbf{M})^{-1}$, where $\mathbf{H} : \mathbb{C}\backslash\Lambda_{\mathbf{H}} \to \mathbb{C}$ is the model of the system to control. In the data-driven case, when $\mathbf{H}(z)$ is not explicitly known but may be evaluated at some frozen values $z_k \in \mathbb{C}$, this definition may be recast as a set of $k = 1, \dots, N$ equations:

$$\mathbf{K}^\star(z_k) = \boldsymbol{\Phi}_k^{-1}\mathbf{M}(z_k)(I - \mathbf{M}(z_k))^{-1}, \tag{7}$$

where $\boldsymbol{\Phi}_k = \mathbf{H}(z_k) \in \mathbb{C}$ is the evaluation of the unknown model at z_k. In an experimental context, one usually considers sampling $\mathbf{H}$ at $z_k = \imath\omega_k$ ($\omega_k \in \mathbb{R}_+$). In this case, $\boldsymbol{\Phi}_k$ is the frequency response of the open-loop system at ω_k. Then, the couple

$$\{z_k, \mathbf{K}^\star(z_k)\}_{k=1}^N, \tag{8}$$

is referred to as the *raw data* for our controller design. Finding a controller $\mathbf{K}$ that *fits* (8) can be considered to be an identification/interpolation problem which may be solved by many approaches. The Loewner framework (Mayo & Antoulas, 2007) allows constructing both a function $\mathbf{K}$ with minimal McMillan degree and realization order $n \leq N$, satisfying conditions (7) or an approximation of it with a realization of order $r < n$.

Remark 3 (*Advantages of The L-DDC*)**.** L-DDC is a combination of determining the ideal controller from frequency-domain data via a reference model and the use of the Loewner framework to construct a reduced order controller. Such an interpolatory-based data-driven control design solves problems faced by practitioners: (i) the controller design is directly obtained using open-loop raw data (8) collected on the experimental setup, (ii) without any optimization process, only linear algebra manipulation, (iii) and without any prior controller structure or order specification (these latter may be automated by a rank revealing factorization). This approach has proven to be effective for digital control (Vuillemin, Kergus, & Poussot-Vassal, 2020) and on experimental application (Poussot-Vassal, Kergus, Kerhervé, et al., 2022). Gosea et al. (2022, sec. 4) provides practical details and didactic examples including infinite dimensional systems.

Remark 4 (*Limitations of The L-DDC*)**.** As a linear controller design, it embeds regular linear limitations. One important has been highlighted

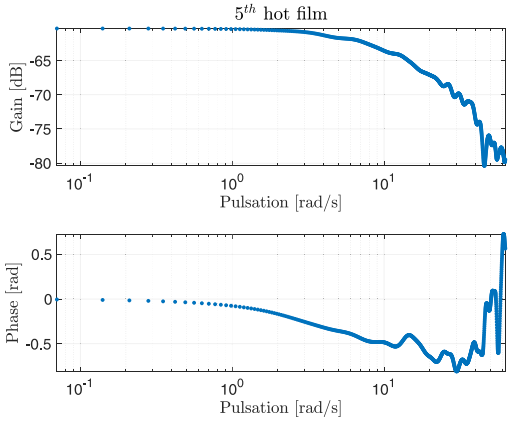

Fig. 11. Frequency response gain and phase diagrams of the data $\boldsymbol{\Phi}_k$ collected during the open-loop experiments.

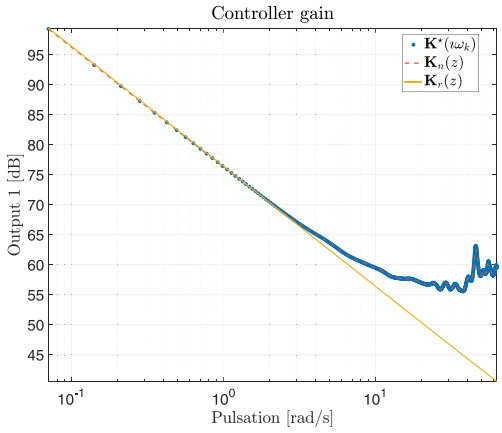

Fig. 12. Bode gain diagrams of the ideal controller data $\mathbf{K}^\star$ (7), its exact interpolated sampled-time controller $\mathbf{K}_n$ and its approximation $\mathbf{K}_r$ with an order $r = 1$.

during the experiments. It concerns the fact that it does not handle actuator limitations, which is in this case works on/off only and are only able to blow air. In presence of an integral action, this may result in stability issues. This point is discussed in Sections 3.2 and 3.3.

3.1.2. Application

The frequency-domain response describing the separated flow dynamics over the flap is first needed. The operating point for this step is a deflection angle $\delta = 24°$ and $U_\infty = 34.5$ m/s, operating point for which the flow is indeed separated at the considered measurement position. Different strategies exist in the literature to identify the input–output dynamics of a system to be controlled. One strategy, described by Dahan, Morgans, and Lardeau (2012) and called Dynamic Linearity, consists in the use of harmonic forcing for the identification. Small amplitude forcing ensures a linear response of the considered flow, and a frequency response can be built. Nevertheless, the use of harmonic forcings on a wide frequency range would be tedious. It is therefore decided to use a logarithmic frequency sweep applied to the valves duty cycle used to derive the frequency-domain response describing the separated flow dynamics. As pointed out by Rouaix et al. (2023) the sweep parameters can influence the response of the flow which dynamics is being identified. In the present case, this sweep is chosen such that the duty cycle evolves in time with a quasi-static rate. Therefore, at any time, the flow can be approximated as forced by a purely harmonic forcing. The actuators command signal $\mathbf{u}(t_k)$ therefore consists in a logarithmic frequency sweep applied to the duty cycle with frequencies ranging from 0.01 Hz to 10 Hz over 180 s. From this input, the fifth hot-film response $\mathbf{y}(t_k)$ is collected. The discrete frequency-domain transfer data from $\mathbf{u}(t_k)$ to $\mathbf{y}(t_k)$ is obtained and denoted $\{\imath\omega_k, \boldsymbol{\Phi}_k\}_{k=1}^N$, where $\omega_k \in \mathbb{R}_+$ is the pulsation and $\boldsymbol{\Phi}_k \in \mathbb{C}$ is the SISO transfer response of the system (orange block in Fig. 9) and $N \in \mathbb{N}$ is the length of the FFT. The data-driven Bode-like diagram is presented in Fig. 11. It exhibits a gain drop around 1 rad/s and a decay in the phase, characteristic of delayed and fractional systems.[2]

Simultaneously with the previous step, the objective closed-loop transfer function $\mathbf{M}$ is defined as a first order model $\mathbf{M}(s) = 1/(s/\omega_0+1)$ where $\omega_0 = 2\pi$ rad/s, is the natural cut-off frequency. We refer to the black dashed lines of Fig. 3, given in the introduction. $\mathbf{M}$ mainly aims at ensuring no steady-sate error (static gain objective set to one).[3] With reference to Eq. (7) we are now ready to compute the ideal controller $\mathbf{K}^\star$ as well as its exact interpolation $\mathbf{K}_n$, where $n = 128$ is automatically selected by the rank revealing factorization embedded in the Loewner process, and its approximations $\mathbf{K}_r$ with an order $r = 1$. After time-domain discretization ($h = 1/100$ s), Fig. 12 illustrates the controller frequency response gains. The implemented linear controller is a pure sampled-time integrator with gain $k = 66.19$ (*i.e.* $\mathbf{K}_r(z) = 66.19/(z-1)$). Obviously, a proportional integral action model may also be identified with a better accuracy. Here we stick to the integral action in view of the nonlinear integral control analysis analyzed in the next section.

Fig. 12 well illustrates that the exact interpolation perfectly matches the data and the approximation with an order $r = 1$ preserves the integral term. Such an observation, coupled with the knowledge of the system input–output positivity property (input blows air and output measures positive values only), motivates the use of a more involved control strategy discussed in the next section.

3.2. Nonlinear positive control design

3.2.1. Idea and principle

Observing that the considered system is stable (indeed, the configuration is an amplification one, but without any instability) and input–output positive (*i.e.* for any nonnegative input $\mathbf{u}$, the output $\mathbf{y}$ is nonnegative), it seems interesting to exploit this property for control purposes. Although not recent (Farina & Rinaldi, 2000), positive systems have recently attracted a lot of attention due to their surprising properties; see e.g. Briat (2013), Ebihara, Peaucelle, and Arzelier (2011). In particular, the theory of (linear) positive systems is playing an essential role in the modeling, the analysis and the control of compartmental systems which include biological, physiological, epidemiological and ecological systems as special cases (Haddad, Chellaboina, & Hui, 2010). Recently, a novel type of integral controller – the Antithetic Integral Controller (AIC) – was introduced in the context of biological control and chemical reaction networks (Briat et al., 2016). The rationale for introducing such a controller was, among others, the derivation of a controller having a positive system representation that could always return a nonnegative control input. It was later proved in Briat (2020) that this nonlinear integral controller enjoyed certain interesting properties which are absent from its linear (*i.e.* non-positive) counterpart. It is also worth mentioning that other nonlinear positive integral controllers exist (Briat, 2020), but the AIC exhibits a lot of the desirable behavioral properties of the usual integral controllers and this is the reason why it is considered here. Indeed, Briat (2020, Thm. 3.6) provides a stability proof of the closed-loop interconnection if the original underlying model is a linear positive one. In fact, those stability conditions coincide, in the worst-case, with the

[2] Note that from this point, model identification may be done in order to apply model-driven method. Here we skip this step to directly go to the control design.

[3] Note that the selection of a first order reference model may be subject to discussions. Here we aim at illustrating the most simple settings. For more details on the choice of $\mathbf{M}$, reader is invited to refer to Kergus (2019).

stability conditions of the standard integral controller, which indicates that using the AIC is not more constraining than using a linear integral controller.

Remark 5 (*Closed-Loop Stability*)**.** In the L-DDC setting, no stability proof can be guaranteed a-priori. This may be checked afterward with specific data-driven techniques (see *e.g.* Kergus (2019, chap. 7) or (Poussot-Vassal, Kergus, & Vuillemin, 2022)). However, one important feature of the positive design by Briat (2020, equation 2.1) is that the closed-loop control of a stable positive system with an AIC ensures local exponential stability, while respecting input signal constraints, under very mild conditions.

3.2.2. Application

The original AIC is given in Briat (2020, equation 2.1) with the following equation set,

$$\begin{array}{rcl} \dot{z}_1(t) & = & \mathbf{r}(t) - \eta z_1(t) z_2(t) \\ \dot{z}_2(t) & = & \mathbf{y}(t) - \eta z_1(t) z_2(t) \\ \mathbf{u}(t_k) & = & k z_1(t) \end{array} . \tag{9}$$

The discretized version (using the backward method) takes the form ($h = 1/100$ s):

$$\begin{array}{rcl} z_1(t_k + h) & = & z_1(t_k) + h\big(\mathbf{r}(t_k) - \eta z_1(t_k) z_2(t_k)\big) \\ z_2(t_k + h) & = & z_2(t_k) + h\big(\mathbf{y}(t_k) - \eta z_1(t_k) z_2(t_k)\big) \\ \mathbf{u}(t_k) & = & k z_1(t_k) \end{array} . \tag{10}$$

Implemented in the real-time environment, user then tunes the values of $k \in \mathbb{R}$ and $\eta \in \mathbb{R}_+$ according to the desired controller. As 10 aims at reproducing the integral action, in our setting, gain k has been set equal to the integral term obtained with the L-DDC approach; *i.e.* $k = 66.19$ (Section 3.1) and $\eta = 300$, used to tend to a pure integral action. We refer to Briat (2020) for further details.

3.3. Flow control experimental results

To validate the proposed reference feedback (linear and nonlinear) integral control, four different type of experiments are carried out. In Section 3.3.1, the lift coefficient C_L with feedback is computed and compare to the uncontrolled one (notice that this is the utilate objective of the control). In Section 3.3.2, the robustness of the control with the deflection angle is analyzed. In Section 3.3.3, the frequency response of the controlled flap is computed and compared to the expected objective. Finally in Section 3.3.4, some considerations on the nonlinear positive controller are discussed.

3.3.1. Lift coefficient gain evaluation (C_L)

Both linear and nonlinear integral controllers have been applied for the same flow conditions. As expected for deflection angles below 13.8°, valves are not opened as the hot-film voltage is above the reference value $\mathbf{r}$. When the hot-film voltage tends to stand below the reference value, valves are opened with a duty cycle determined by the controller (this is typically the case when flap angle is increased). As an effect, the hot-film voltage is maintained at the reference value thanks to the feedback control action. The closed-loop control effect on the flow dynamics stabilization can be observed in Fig. 13, presenting the evolution of the 5th hot-film RMS voltage against the flap deflection angle δ. The RMS voltage is constant for all the angles of attack for which the closed-loop control is indeed active.

As presented in the introduction, Fig. 2 highlights the benefit of control on the lift coefficient C_L increase. For $\delta < 13.8°$, both uncontrolled and controlled flow present the same lift coefficient, as in both cases valves are not opened. However, for $\delta > 13.8°$, curves for the uncontrolled and controlled cases do not superimpose anymore. The lift coefficient in the controlled case is higher than the one of the uncontrolled case. Regarding the controlled case, the linear evolution of C_L is extended up to $\delta = 24°$. Between $\delta = 24°$ and $\delta = 26°$, C_L is

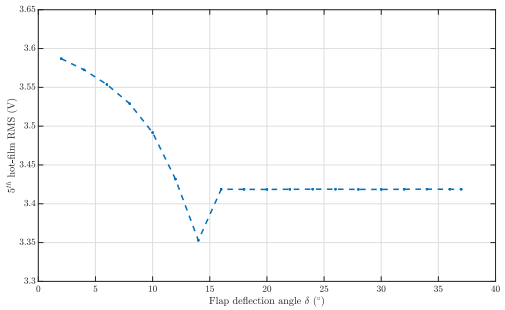

Fig. 13. Evolution of the 5th hot-film RMS voltage (V) against the deflection angle δ (°) ($U_\infty = 34.5$ m/s) in the controlled case.

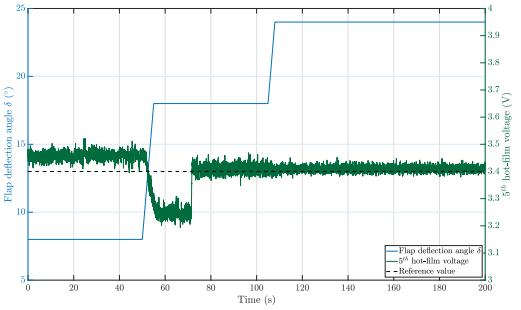

Fig. 14. Evolution of the flap deflection angle against time (left axis) and evolution of both the 5th hot-film voltage and reference value (right axis) against time for the linear controller.

reduced drastically. This phenomenon is due to the apparition of flow separation at the flap trailing edge. This flow separation does not spread over the entire flap as the control counters it and hold it at the flap trailing edge.[4] These results can also be observed in the analysis of the pressure coefficient evolution in both the uncontrolled and controlled flow cases. As both the linear controller and the nonlinear positive controller have been applied with the same reference value on the hot-film, both control cases yielded the same results on the lift and pressure coefficients.

3.3.2. Robustness to flap angle deflection (δ)

In order to test the controllers robustness against the deflection angle, measurements were also performed with varying angles. In a given experiment, flap deflection angle was varied from $\delta = 8°$ to $\delta = 18°$ and to $\delta = 24°$. The flap deflection angle varied from 8° to 18° induces the apparition of the separated flow at the sensor used for the closed-loop control implementation. Further deflecting the flap angle from 18° to 24° induces a strengthening of the recirculation flow intensity inside the flow separated area. The linear controller shows its limits due to its linear integral behavior and the fact that it does not handle the positiveness of the system. As valves are not opened for $\delta = 8°$, the linear controller takes into account the error and therefore accumulates an integral error. In that sense, when the deflection angle increases to $\delta = 18°$ for which valves have to be open, the controller effect is in the wrong direction. As observed in Fig. 14, once the linear controller has overcome the accumulated error, the controller is robust to the deflection angle variation from 18° to 24°.

As such an error could not be tolerated in real application, a way to circumvent it would be to implement an anti-windup on the linear controller. This may be done at a price of more involved calculus, usually

[4] This observation motivates future investigations involving additional sensors and a more involved multi-input control.

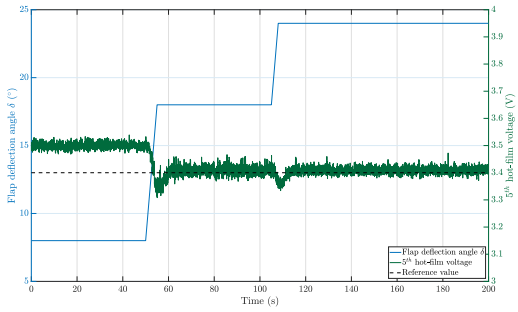

Fig. 15. Evolution of the flap deflection angle against time (left axis) and evolution of both the 5th hot-film voltage and reference value (right axis) against time for the positive controller.

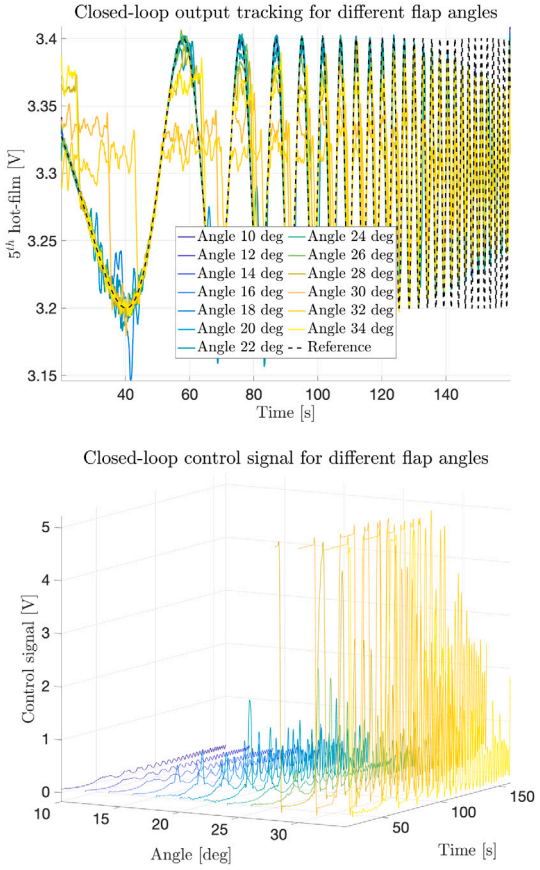

Fig. 16. Linear controller action for frozen flap deflection angles δ. Top: reference tracking performances. Bottom: produced control signals.

involving a model, while here, the pure data-driven setup is employed. However, we proved in these experiments than an other simple and efficient way to deal with this integral behavior is to implement a nonlinear positive controller instead. As described in Fig. 15, the delay resulting from the integral error issue totally vanishes considering this controller. In addition to that, in this setup, the input output stability is formally guaranteed.

3.3.3. Frequency-domain responses

In addition, to compute the frequency response of the closed-loop control and ensure that the closed-loop performances meet the reference model **M** objective, a sinus around the tracking value, with frequency sweep signal is given as reference. The time-domain responses of the output and control signals are reported in Fig. 16.

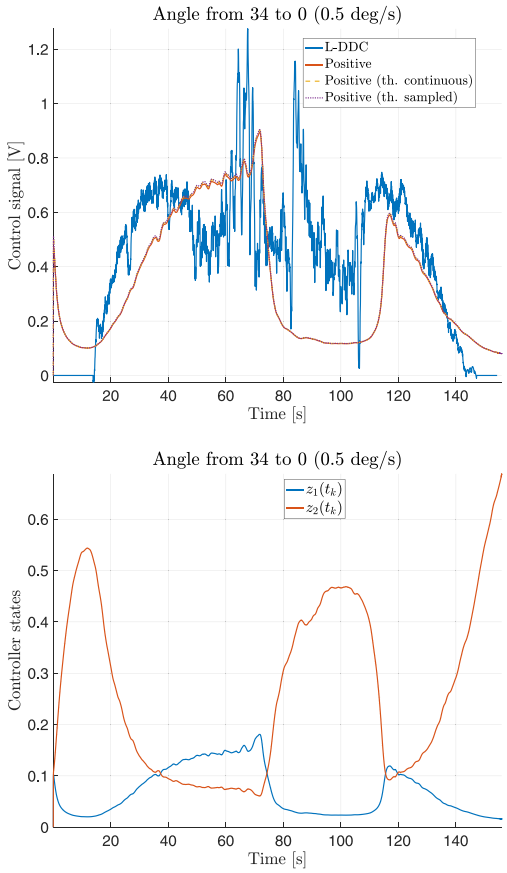

Fig. 17. Experiment where flap angle δ travels from 34 degrees to 0 degree. Top: control signal of the linear and nonlinear experimental controllers and theoretical nonlinear continuous and sampled control. Bottom: sampled-time positive controller internal states.

The top frame allows computing the frequency response diagram given in the introduction, illustrating that the performances are very close to the expected one fixed by **M** (see Fig. 3). On the bottom frame, the control signal of the linear controller shows to reach the saturation quite often, which is an other motivation for the nonlinear positive control.

3.3.4. Further remark on the nonlinear positive control

Finally, a time-domain experiment where the reference is fixed but the flap deflection angle δ travels from 0 to 34 and 34 to 0 degree with a speed rate of 0.5 deg/s (5 s hold at the beginning, middle and end) is performed (we compare here both strategies). Fig. 17 (top) shows the control signal actuation for both the linear and nonlinear (positive) controllers. First it illustrates the fact that the positive controller avoids the saturation while the linear one tends to often reach then. In the same frame, for the positive control law, we compare the experimental control signal (solid orange) with the reconstructed theoretical continuous 9 (dashed yellow) and sampled 10 (dashed violet) when fed by the experimental data. Both lead to a perfect match which confirms the good implementation. Then Fig. 17 (bottom) illustrates the positive sampled-time controller internal states, which both remain, as expected, positives.

4. Conclusions

This paper presents experimental validations of active closed-loop control of flow separation over a plain flap. We numerically and experimentally demonstrate that flow separation may be improved by mean

of a (SISO) reference signal tracking feedback control architecture, involving a controller with integral action. We also proposed two control laws: first *(i)* a linear one where the integral gain is computed via a direct data-driven approach, and second, *(ii)* a nonlinear positive controller to account for the system limitations, using the very same gain.

Both strategies enabled to maintain a reference voltage value on the objective hot-film placed at the flap mid-chord. The latter reference, being calculated based on the flow separation observation. Both controllers efficiency were assessed through lift coefficient calculations derived from pressure measurements (Fig. 2). Their robustness to the flap deflection angle was also tested through experiments, during which the flap angle was continuously varied. Based on this first successful demonstration, future works could focus on the controllers parametrization with respect to the flow conditions, such as the freestream velocity and could provide a complete analysis of the two controllers robustness. Additionally, we demonstrate that the expected theoretical performances were recovered experimentally. The most significant advantage of these control techniques lies in the simplicity of their application, which is of importance for practitioners in view of experimentation and implementation.

Application of such controllers could be extended to other flow control problems in future works, as well as more detailed validations. In addition, a comparison with a digital twin of the wind tunnel remains and interesting challenge for research.

CRediT authorship contribution statement

T. Arnoult: Writing – review & editing, Writing – original draft, Software, Investigation, Conceptualization. **G. Acher:** Software, Investigation. **V. Nowinski:** Writing – review & editing, Writing – original draft, Software, Investigation. **P. Vuillemin:** Software, Investigation. **C. Briat:** Writing – original draft, Investigation, Conceptualization. **P. Pernod:** Supervision. **C. Ghouila-Houri:** Supervision. **A. Talbi:** Supervision. **E. Garnier:** Supervision, Resources. **C. Poussot-Vassal:** Writing – review & editing, Writing – original draft, Visualization, Supervision, Software, Resources, Project administration, Methodology, Investigation, Funding acquisition, Conceptualization.

Declaration of competing interest

The authors declare that they have no known competing financial interests or personal relationships that could have appeared to influence the work reported in this paper.

Acknowledgments

This work was funded by the French National Research Agency (ANR), France in the framework of the ANR ASTRID MATURATION CAMELOTT-MATVAL Project. It is supported by the regional platform CONTRAERO, France in the framework of the CPER ELSAT 2020 Project. The Defence Innovation Agency (DIA), France has also financially sustained this work. The authors also thank RENATECH, the French national nanofabrication network, and FEDER. It has also been financed by the ONERA research project FluiDyCon, Fluid Dynamical Control, France.

References

Allan, B., Juang, J. N., Raney, D., Seifert, A., Pack, L., & Brown, D. (2000). *Closed-loop separation control using oscillatory flow excitation: Technical report 2000–32*, NASA.

Becker, R., King, R., Petz, R., & Nitsche, W. (2007). Adaptive closed-loop separation control on a high-lift configuration using extremum seeking. *AIAA Journal*, *45*(6), 1382–1392. http://dx.doi.org/10.2514/1.24941.

Benard, N., Cattafesta, L. N., Moreau, E., Griffin, J., & Bonnet, J. P. (2011). On the benefits of hysteresis effects for closed-loop separation control using plasma actuation. *Physics of Fluids*, *23*(8), Article 083601. http://dx.doi.org/10.1063/1.3614482.

Benard, N., Moreau, E., Griffin, J., & Cattafesta III, L. N. (2010). Slope seeking for autonomous lift improvement by plasma surface discharge. *Experiments in Fluids*, *48*(5), 791–808. http://dx.doi.org/10.1007/s00348-009-0767-6.

Briat, C. (2013). Robust stability and stabilization of uncertain linear positive systems via integral linear constraints - L_1- and L_∞-gains characterizations. *International Journal of Robust and Nonlinear Control*, *23*(17), 1932–1954.

Briat, C. (2020). A Biology-Inspired Approach to the Positive Integral Control of Positive Systems: The Antithetic, Exponential, and Logistic Integral Controllers. *SIAM Journal on Applied Dynamical Systems*, *19*(1), 619–664.

Briat, C., Gupta, A., & Khammash, M. (2016). Antithetic integral feedback ensures robust perfect adaptation in noisy biomolecular networks. *Cell Systems*, *2*(1), 15–26.

Brunton, S. L., & Noack, B. R. (2015). Closed-loop turbulence control: Progress and challenges. *Applied Mechanics Reviews*, *67*(5), Article 050801. http://dx.doi.org/10.1115/1.4031175.

Chabert, T. (2014). *Contrôle expérimental en boucle fermée du décollement sur un volet* (Ph.D. thesis), Université Pierre et Marie Curie.

Chabert, T., Dandois, J., & Garnier, E. (2014). Experimental closed-loop control of flow separation over a plain flap using slope seeking. *Experiments in Fluids*, *55*(8), 1797. http://dx.doi.org/10.1007/s00348-014-1797-2.

Chabert, T., Dandois, J., Garnier, E., & Jacquin, L. (2014). Experimental detection of flow separation over a plain flap by wall shear stress analysis with and without steady blowing. *Comptes Rendus Mécanique*, *342*(6–7), 389–402. http://dx.doi.org/10.1016/j.crme.2014.01.013.

Dahan, J. A., Morgans, A. S., & Lardeau, S. (2012). Feedback control for form-drag reduction on a bluff body with a blunt trailing edge. *Journal of Fluid Mechanics*, *704*, 360–387. http://dx.doi.org/10.1017/jfm.2012.246.

Dandois, J., & Pamart, P. Y. (2013). NARX modeling and extremum-seeking control of a separation (6). (p. 14).

Debien, A., von Krbek, K. A. F. F., Mazellier, N., Duriez, T., Cordier, L., Noack, B. R., et al. (2016). Closed-loop separation control over a sharp edge ramp using genetic programming. *Experiments in Fluids*, *57*(3), 40. http://dx.doi.org/10.1007/s00348-016-2126-8.

Ebihara, Y., Peaucelle, D., & Arzelier, D. (2011). L_1 Gain analysis of linear positive systems and its applications. In *50th conference on decision and control, Orlando, Florida, USA* (pp. 4029–4034).

Farina, L., & Rinaldi, S. (2000). *Positive linear systems: Theory and applications*. John Wiley & Sons.

Feingesicht, M., Polyakov, A., Kerhervé, F., & Richard, J. P. (2017). Sliding mode control for turbulent flows. *IFAC-PapersOnLine*, *50*(1), 2690–2695. http://dx.doi.org/10.1016/j.ifacol.2017.08.554.

Formentin, S., van Heusden, K., & Karimi, A. (2014). A comparison of model-based and data-driven controller tuning. *International Journal of Adaptive Control and Signal Processing*, *28*(10), 882–897.

Garwon, M., Darmadi, L. H., Urzynicok, F., Barwolff, G., & King, R. (2003). Adaptive control of separated flows. In *2003 European control conference* (pp. 3231–3236). Cambridge, UK: IEEE, http://dx.doi.org/10.23919/ECC.2003.7086537.

Gautier, N., Aider, J.-L., Duriez, T., Noack, B. R., Segond, M., & Abel, M. (2015). Closed-loop separation control using machine learning. *Journal of Fluid Mechanics*, *770*, 442–457. http://dx.doi.org/10.1017/jfm.2015.95.

Gosea, V., Poussot-Vassal, C., & Antoulas, A. (2022). Data-driven modeling and control of large-scale dynamical systems in the Loewner framework. *Handbook of Numerical Analysis*, *23*(Numerical Control: Part A), 499–530.

Greenblatt, D., & Wygnanski, I. J. (2000). The control of #ow separation by periodic excitation. *Progress in Aerospace Sciences*, 59.

Haddad, W. M., Chellaboina, V., & Hui, Q. (2010). *Nonnegative and compartmental dynamical systems*. 41 William Street, Princeton, USA: Princeton University Press.

Gad-el Hak, M. (2000). *Flow control: Passive, active, and reactive flow management*. Cambridge: Cambridge University Press, OCLC: 247967659.

Henning, L., & King, R. (2007). Robust multivariable closed-loop control of a turbulent backward-facing step flow. *Journal of Aircraft*, *44*(1), 201–208. http://dx.doi.org/10.2514/1.22934.

Hoerner, S. F. (1985). In H. V. Borst (Ed.), *Fluid-dynamics lift: Practical information on aerodynamic and hydrodynamics lift*. Brick Town, N.J., Hoerner.

Kergus, P. (2019). *Data-driven model reference control in the frequency-domain from model reference selection to controller validation* (Ph.D. thesis), Toulouse, France: Onera, ISAE, Toulouse University.

Killingsworth, N. J., & Krstic, M. (2006). PID tuning using extremum seeking: online, model-free performance optimization. *IEEE Control Systems*, *26*(1), 70–79. http://dx.doi.org/10.1109/MCS.2006.1580155.

King, R., Heinz, N., Bauer, M., Grund, T., & Nitsche, W. (2013). Flight and wind-tunnel tests of closed-loop active flow control. *Journal of Aircraft*, *50*(5), 1605–1614. http://dx.doi.org/10.2514/1.C032129.

Lee, B., Kim, M., Choi, B., Kim, C., Kim, H. J., & Jung, K. J. (2013). Closed-loop active flow control of stall separation using synthetic jets. In *31st AIAA applied aerodynamics conference*. San Diego, CA: American Institute of Aeronautics and Astronautics, http://dx.doi.org/10.2514/6.2013-2925.

Lombardi, A. J., Bowles, P. O., & Corke, T. C. (2013). Closed-loop dynamic stall control using a plasma actuator. *AIAA Journal*, *51*(5), 1130–1141. http://dx.doi.org/10.2514/1.J051988.

Mayo, A. J., & Antoulas, A. C. (2007). A framework for the solution of the generalized realization problem. *Linear Algebra and its Applications*, *425*(2), 634–662.

Packard, N., & Bons, J. (2012). Closed-loop separation control of unsteady flow on an airfoil at low Reynolds number. In *50th AIAA aerospace sciences meeting including the new horizons forum and aerospace exposition*. Nashville, Tennessee: American Institute of Aeronautics and Astronautics, http://dx.doi.org/10.2514/6.2012-754.

Pastoor, M., Henning, L., Noack, B. R., King, R., & Tadmor, G. (2008). Feedback shear layer control for bluff body drag reduction. *Journal of Fluid Mechanics*, *608*, 161–196. http://dx.doi.org/10.1017/S0022112008002073.

Pinier, J. T., Ausseur, J. M., Glauser, M. N., & Higuchi, H. (2007). Proportional closed-loop feedback control of flow separation. *AIAA Journal*, *45*(1), 181–190. http://dx.doi.org/10.2514/1.23465.

Poggie, J., Tilmann, C. P., Flick, P. M., Silkey, J. S., Osbourne, B. A., Ervin, G., et al. (2010). Closed-loop stall control system. *Journal of Aircraft*, *47*(5), 1747–1755. http://dx.doi.org/10.2514/1.C000262.

Poussot-Vassal, C., Kergus, P., Kerhervé, F., Sipp, D., & Cordier, L. (2022). Interpolatory-based data-driven pulsed fluidic actuator control design and experimental validation. *IEEE Transactions on Control Systems Technology*, *30*(2), 852–859.

Poussot-Vassal, C., Kergus, P., & Vuillemin, P. (2022). In C. Beattie, P. Benner, M. Embree, S. Gugercin, & S. Lefteriu (Eds.), *Realization and model reduction of dynamical systems, A Festschrift in Honor of the 70th Birthday of Thanos Antoulas* (pp. 353–371). Springer, Chapter Interpolation-based irrational model control design and stability analys.

Rethmel, C., Little, J., Takashima, K., Sinha, A., Adamovich, I., & Samimy, M. (2011). Flow separation control using nanosecond pulse driven DBD plasma actuators. *International Journal of Flow Control*, *3*(4), 213–232. http://dx.doi.org/10.1260/1756-8250.3.4.213.

Rouaix, C., Jiménez-Navarro, C., Carvalho, M., Raibaudo, C., Abou-Khalil, J., Marouf, A., et al. (2023). Electroactive morphing effects on the aerodynamic performance through wobulation around an A320 wing with vibrating trailing edge at high Reynolds number. *Journal of Fluids and Structures*, *123*, Article 104016. http://dx.doi.org/10.1016/j.jfluidstructs.2023.104016.

Shaqarin, T., Braud, C., Coudert, S., & Stanislas, M. (2013). Open and closed-loop experiments to identify the separated flow dynamics of a thick turbulent boundary layer. *Experiments in Fluids*, *54*(2), 1448. http://dx.doi.org/10.1007/s00348-012-1448-4.

Shimomura, S., Sekimoto, S., Oyama, A., Fujii, K., & Nishida, H. (2020). Experimental study on application of distributed deep reinforcement learning to closed-loop flow separation control over an airfoil. In *AIAA scitech 2020 forum*. Orlando, FL: American Institute of Aeronautics and Astronautics, http://dx.doi.org/10.2514/6.2020-0579.

Tewes, P., Wygnanski, I., & Washburn, A. E. (2011). Feedback-controlled forcefully attached flow on a stalled airfoil. *Journal of Aircraft*, *48*(3), 940–951. http://dx.doi.org/10.2514/1.C031168.

Tian, Y., Cattafesta, L., & Mittal, R. (2006). Adaptive control of separated flow. In *44th AIAA aerospace sciences meeting and exhibit*. Reno, Nevada: American Institute of Aeronautics and Astronautics, http://dx.doi.org/10.2514/6.2006-1401.

Troshin, V., & Seifert, A. (2013). Performance recovery of a thick turbulent airfoil using a distributed closed-loop flow control system. *Experiments in Fluids*, *54*(1), 1443. http://dx.doi.org/10.1007/s00348-012-1443-9.

Vuillemin, P., Kergus, P., & Poussot-Vassal, C. (2020). Hybrid Loewner data driven control. In *Proceedings of the IFAC world congress*. Berlin, Germany.

Ziegler, J., & Nichols, N. (1942). Optimum settings for automatic controllers. *Transactions of the ASME*, *64*, 759–768.